Evolution of Low-Level Angular Momentum in the 2 June 1995 Dimmitt, Texas, Tornado Cyclone

ERIK N. RASMUSSEN

Cooperative Institute for Mesoscale Meteorological Studies, National Severe Storms Laboratory, and University of Oklahoma, Norman, Oklahoma

JERRY M. STRAKA

University of Oklahoma, Norman, Oklahoma

(Manuscript received 2 February 2005, in final form 8 March 2006)

ABSTRACT

The life cycle of the 2 June 1995 Dimmitt, Texas, tornado cyclone, observed during the Verification of the Origins of Rotation in Tornadoes Experiment (VORTEX), is described. The tornado cyclone here is defined as a significantly axisymmetric flow larger than the visible tornado and characterized by increasing angular momentum with increasing radius. Its life cycle included three phases with somewhat differing evolution of angular momentum, herein called intensifying, transition, and weakening. During the intensifying stage, the funnel and debris cloud gradually increased in size. The azimuthally averaged secondary circulation of the larger-scale tornado cyclone, as determined using high-resolution single-Doppler data obtained by a mobile radar, was primarily inward and upward, consistent with the presence of a wall cloud outside the tornado. The azimuthally averaged angular momentum increased monotonically away from the tornado, so inward advection allowed the angular momentum to increase slowly with time in part of the tornado cyclone. During the transition phase, downdrafts began to occur within the tornado cyclone. The transport of angular momentum by the secondary circulation nearly was offset by eddy flux convergence of angular momentum so that the azimuthally averaged angular momentum tendency was only weakly negative at most radii. The tornado was visually impressive during this stage, featuring a 400-m diameter debris cloud extending to cloud base, while the surrounding wall cloud shrank and eroded. During the weakening phase, the funnel and debris cloud gradually shrank, and the funnel went through a rope stage prior to disappearing. The weakening phase was characterized by extensive downdrafts at all radii outside the tornado, and large-scale near-ground outflow as observed by mobile mesonet systems in a portion of the tornado cyclone. The secondary circulation acted to transport smaller angular momentum downward from aloft, and outward along the ground. All terms of the angular momentum budget became negative throughout most of the low-level (0–800-m AGL) tornado cyclone during the weakening phase. Several hypotheses for this evolution are evaluated, including changes in water loading in the tornado cyclone, cooling of the near-ground air, and the distribution of tangential velocity with height with its concomitant influence on the nonhydrostatic vertical pressure gradient force.

1. Introduction

On 2 June 1995, a significant tornado occurred near Dimmitt, Texas, and was observed by the Verification of the Origins of Rotation in Tornadoes Experiment (VORTEX; Rasmussen et al. 1994) and documented comprehensively by Wurman and Gill (2000). The Wurman and Gill study focused on the evolution of the tornado; herein we examine the evolution of the vortex in which the tornado was embedded, called the tornado cyclone (TC). We define the TC as that region surrounding the tornado in which angular momentum generally increases with increasing radius and a certain degree of axisymmetry is maintained. The angular momentum budget of this TC is analyzed, and its evolution is interpreted in the context of near-ground virtual potential temperature changes, reflectivity changes, and the evolution of the swirl at somewhat larger scales

Corresponding author address: Dr. Erik N. Rasmussen, P.O. Box 267, Mesa, CO 81643.
E-mail: rasm1@wildblue.net

DOI: 10.1175/JAS3829.1

than the tornado cyclone. The angular momentum budget analysis is described in section 2, and evolution is summarized for each phase of tornado cyclone evolution. The phases, denoted for convenience as intensifying, transition, and weakening are documented in sections 3, 4, and 5, respectively. In each section, mobile mesonet and mobile Doppler data are combined to document the near-ground wind and thermodynamics structure of the tornado cyclone, and mobile Doppler and photographic data are combined to understand the vertical reflectivity structure of the tornado cyclone and its relation to precipitation [a similar analysis of a Colorado tornado is reported in Wakimoto and Martner (1992)]. Further, mobile Doppler data are utilized to compute azimuthally averaged angular momentum and its budget in the tornado cyclone. The net angular momentum was generally very slowly increasing during the intensifying phase, nearly steady during the transition phase, and decreasing during the weakening phase.

Three hypotheses are evaluated regarding the observed evolution of angular momentum in the tornado cyclone. First, the evolution of the TC could have been influenced by changes in the state of the TC low-level flow as explored by Markowski et al. (2002, 2003). This is evaluated by examining maps of mobile mesonet data (Straka et al. 1996) near to the TC. A second hypothesis investigated herein is that the evolution of the TC is due to changes in the swirl and updraft in the parent mesocyclone. The near-ground TC should contain downdrafts if the nonhydrostatic vertical pressure gradient force is downward-directed owing to maximum swirl near the ground (e.g., Klemp and Rotunno 1983) and vice versa. Further, it should be expected that if the parent updraft weakens, $\partial w/\partial z$ in the vortex should weaken resulting in less stretching of vertical vorticity of parcels in the vortex. The third hypothesis is that the vertical draft structure of the TC evolves in response to water loading as measured by average reflectivity. The first hypothesis is discussed along with presentation of the angular momentum evolution in sections 3 to 5 and the latter two are evaluated in sections 6 and 7. The findings of this paper are further discussed and summarized in section 8.

2. Evolution of angular momentum

To establish a method for evaluating angular momentum in a TC, we first examine the governing equation for angular momentum. The incompressible Navier–Stokes equation for tangential velocity, in cylindrical coordinates, is

$$\frac{\partial v}{\partial t} + u\frac{\partial v}{\partial r} + \frac{v}{r}\frac{\partial v}{\partial \lambda} + w\frac{\partial v}{\partial z} + \frac{uv}{r} - \frac{1}{\rho r}\frac{\partial p}{\partial \lambda} = \nu\left[\frac{\partial}{\partial r}\left(\frac{1}{r}\frac{\partial rv}{\partial r}\right) + \frac{\partial^2 v}{\partial z^2}\right], \quad (1)$$

where $\mathbf{V} = (u, v, w)$ components in the (r, λ, z) coordinates, and ν is the kinematic viscosity. In this analysis, the kinematic viscosity is comprised primarily of eddy viscosity, and the entire right-hand side of (1) will be replaced by the symbol K. An equation for angular momentum, $M = vr$, is obtained from (1) through multiplication by r and substitution, giving

$$\frac{\partial M}{\partial t} + u\frac{\partial M}{\partial r} + \frac{M}{r^2}\frac{\partial M}{\partial \lambda} + w\frac{\partial M}{\partial z} - \frac{1}{\rho}\frac{\partial p}{\partial \lambda} - Kr = 0. \quad (2)$$

This equation expresses the principal of conservation of angular momentum in the absence of azimuthal pressure forces and viscous dissipation. It is of interest in this study to separate the azimuthal average parts of the angular momentum budget from those associated with asymmetries and other eddy effects. Letting overbars represent azimuthal averages, and primes departures from those averages, after application of the continuity equation, we obtain

$$\frac{\partial \overline{M}}{\partial t} = -\frac{1}{r}\frac{\partial (r\overline{u}\,\overline{M})}{\partial r} - \frac{\partial (\overline{w}\,\overline{M})}{\partial z} - \frac{1}{r}\frac{\partial (r\overline{u'M'})}{\partial r} - \frac{\partial}{\partial z}(\overline{w'M'}) + Kr. \quad (3)$$

It is possible to obtain estimates of azimuthally averaged tangential and radial flow components using high-resolution single-Doppler velocity data. Examples of these techniques include Lee et al. (1994) and Bluestein et al. (2003). A similar method was used in this study, but only the zeroth moment (azimuthal average) of tangential and radial winds was computed. The same caveats apply to this study as described in those papers cited above; however, the present study does not attempt to deduce any of the asymmetric components of the flow from the single-Doppler data. Upon removal of the translation of the vortex (to correctly align features in the vertical), the vertical component of velocity can then be determined by integrating the equation for mass continuity; in this case utilizing the Boussinesq approximation. In this study, we do not utilize data from small radii where debris centrifuging could contaminate estimates of radial velocity (e.g., Wurman and Gill 2000, p. 2161). Ground clutter targets were edited from the dataset. Finally, radial flow deep-

ens in the TC (compared to the tornado) allowing the radar to sufficiently resolve the radial component.

Eight volume scans containing the Dimmitt TC were obtained with mobile Doppler radar during the period 0102:52 to 0115:17 UTC (in this study, all mobile Doppler observation times refer to the time that radar observed the tornado itself at 0° nominal elevation angle). Thus, sufficient data exist to evaluate (3) rewritten as

$$\frac{\partial \overline{M}}{\partial t} + \frac{\partial \overline{uM}}{\partial r} + \frac{\partial \overline{wM}}{\partial z} = R, \tag{4}$$

where R, the residual, is the horizontal and vertical convergence of the eddy angular momentum flux and viscous dissipation of angular momentum, the latter only being important in the surface layer. The data are not sufficient to evaluate the separate contributions to the residual.

To compute the azimuthally averaged tangential and radial velocity components, it was necessary to assume a location of the vortex center. In examining the raw Doppler velocity fields, it was apparent that the center of the tornado cyclone was approximately collocated with the center of the tornado, the latter, which was revealed by the presence of an echo-weak hole (e.g., Wurman and Gill 2000). It would be erroneous to assume that at least the inner portion of the tornado cyclone was not approximately collocated with the outer portion of the tornado. To assess the sensitivity of the azimuthal averages to uncertainty in the chosen center location, the computations were repeated 100 times with the center positioned randomly within the tornado echo-weak hole, and this test was conducted at each vertical data level. The results are shown in Fig. 1, and it is safe to assume that the actual uncertainties are near the bottoms of the ranges shown because in practice the center location can be selected very near to the center of the tornado echo-weak hole, and not at locations near the edge of the tornado echo-weak hole, which had a diameter of 100–300 m. The uncertainties in tangential velocity were typically <0.5 m s^{-1}, and generally $<2\%$ of the tangential velocity at any height or radius. The uncertainties in radial velocity were typically <0.5 m s^{-1} as well except at small radii. There is no reason to believe that the uncertainties are associated with systematic bias that could significantly alter the general pattern of the secondary (radial-vertical) circulation.

The terms of this equation will be examined in detail in sections 4, 5, and 6. First, we establish the overall evolution of the angular momentum in the Dimmitt TC. As noted in the introduction, a dynamical definition of the TC is developed: that region surrounding the tornado in which angular momentum generally increases with increasing radius and a certain degree of axisymmetry is maintained. Herein, the criterion MAE/$\bar{v} < 0.35$ is used as the measure of approximate axisymmetry, where $\bar{v}$ is the azimuthally averaged tangential velocity, and MAE is the mean absolute error of the fit of Doppler velocity to equation for $\bar{v}$. The value 0.35 was selected somewhat arbitrarily by examining the raw Doppler velocity displays for the loss of axisymmetry in the vortex, and then examining the MAE at those radii where axisymmetry was lost.

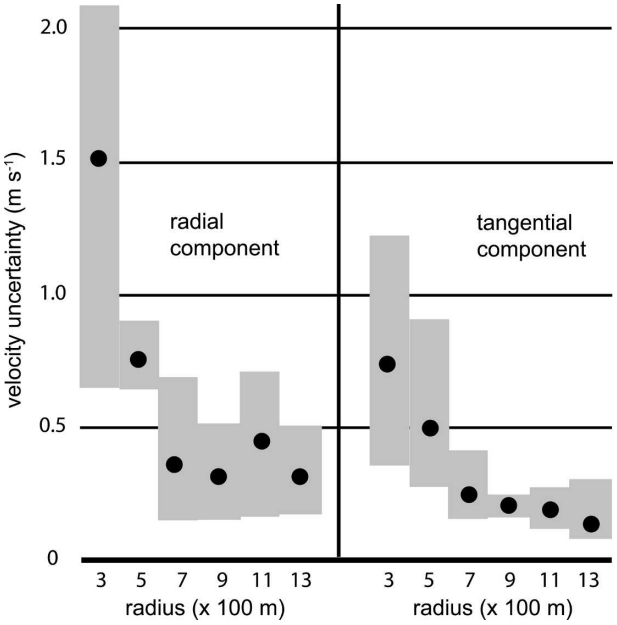

FIG. 1. Graph of uncertainty in azimuthally averaged velocity components. Gray bars give the range of uncertainty found at all heights among 100 random center positions (see text for details). The black dot is the average uncertainty among all trials.

Figure 2 shows $\overline{M}$ as a function of time and radius for four heights in the Dimmitt TC based on the eight volumetric observations made with mobile Doppler radar. In this discussion, time is referenced to the first appearance of the visible tornado. For the first six min of its existence, the TC was not observed with mobile Doppler radar as the vehicle was being moved to a position closer to the tornado. In general, the TC initially was larger at 200 m AGL[1] than above or below that height.

[1] These are nominal heights rounded for the simplicity of discussion. In the actual data and in all calculations, 0 m AGL corresponded to 0° antenna elevation; 200 m AGL to 4°, 400 m AGL to 8°, 600 m AGL to 10°, and 800 m AGL to 14°. Thus the actual height of the data depended on the distance to the tornado which was typically about 3000 m. The bias in the antenna elevation angle is not known; however, the ground clutter was very prominent at 0° elevation, and the terrain is very flat near Dimmitt.

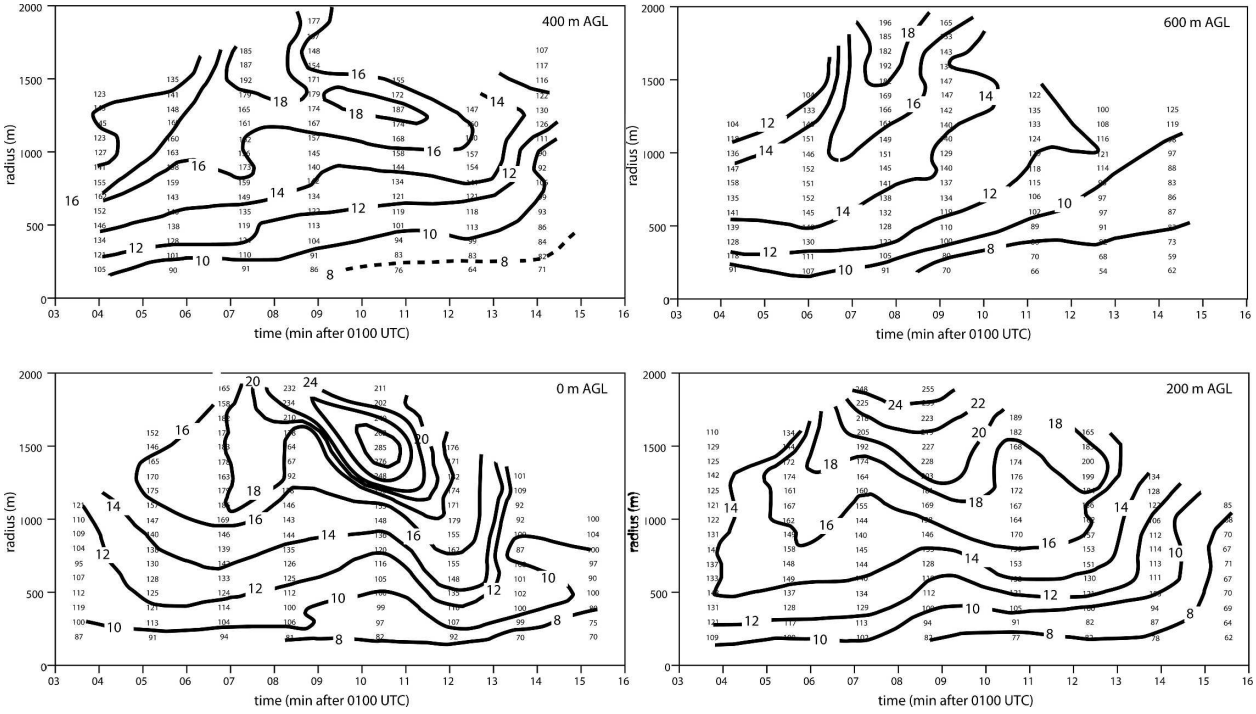

FIG. 2. Time series of azimuthally averaged angular momentum $\times 10^3$ m^2 s^{-1}; $\overline{M}$ as a function of radius at four heights as labeled, derived from mobile single-Doppler data. Data are plotted only if MAE/$\overline{v} < 0.35$.

It grew to become larger than the radius of the analysis domain (2000 m) for several minutes between 0107 and 0111 UTC. The TC then decreased in size, with this shrinking of the axially quasi-symmetric region commencing at all heights near the start of the weakening phase (~0111 UTC). The intensity of the TC near the ground, as measured by $\overline{M}$, generally increased with time during the period 0103–0107 UTC, was relatively constant between 0107 and 0111 UTC, and then decreased with time thereafter. At all heights, there is an $\overline{M}$ maximum that moves from ~1000 m radius at early times, to 1500–2000 m radius during the transition period, and then back toward smaller radii during the weakening phase. During the first half of the period, there is a tendency for $\overline{M}$ to be slightly larger aloft than near the ground, while during the weakening stage $\overline{M}$ decreased more rapidly aloft than at the ground, leading to $\overline{M}$ decreasing with height.

Other features of the evolution of $\overline{M}$ are worth noting. There is evidence that, in the lowest 800 m, a maximum in $\overline{M}$ descended near the periphery of the TC between 0108 and 0111 UTC. At 0108, there was a maximum in $\overline{M}$ at 600 m AGL. At 0109, this maximum appeared to be located near 200–400 m AGL, and at 0110 a strong maximum appeared near the ground at large radii. With time, this weakening maximum moved toward smaller radii at 0 m AGL. These general features and trends in the azimuthally averaged angular momentum are examined in more detail in the following three sections.

3. Intensification period prior to 0107 UTC

As shown in the previous section, the mobile Doppler data indicate a peak in $\overline{M}$ at around 0107 UTC. Therefore, we will characterize the period prior to 0107 UTC as the intensification period. The use of these labels (intensification, transition, and weakening) should not be construed as meaning that most TCs go through similar evolution of angular momentum. "Typical" features and evolution can only be determined through additional case studies.

The first mobile Doppler data were collected at 0103:32 UTC, and data from ~0105 UTC will be utilized to illustrate the tornado and tornado cyclone morphology during the intensification period. A high-quality video segment was being shot at that time by the CAM-1 VORTEX team from a position ~12 km east-northeast of the tornado. The image (Fig. 2) was scaled using the techniques described in Rasmussen et al. (2003). Three landmarks were used for scaling, with an uncertainty in angular displacement of <0.1°. The uncertainty in distance from the camera to tornado is ~250 m. Image scaling was verified by scaling images

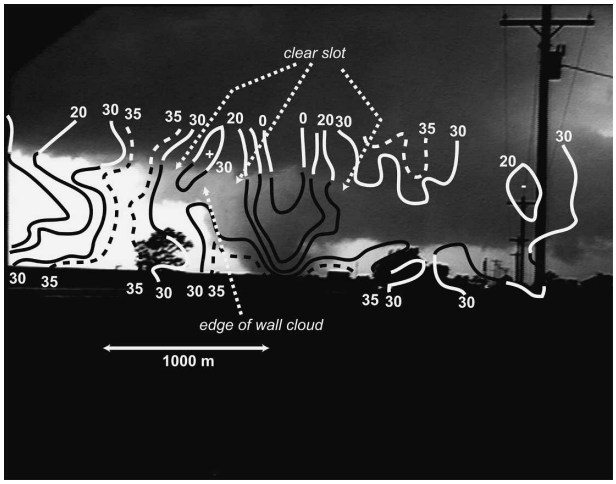

FIG. 3. Image of the Dimmitt tornado at 0104:56 UTC digitized from SVHS video shot by the VORTEX CAM-1 team from east-northeast of the tornado. Contours are mobile Doppler reflectivity (dBZ; 10-dBZ interval with additional dashed contour at 35 dBZ) in the plane of the photograph at the distance of the tornado. The labeled heavy arrow below the horizon indicates length scale in the plane containing the tornado.

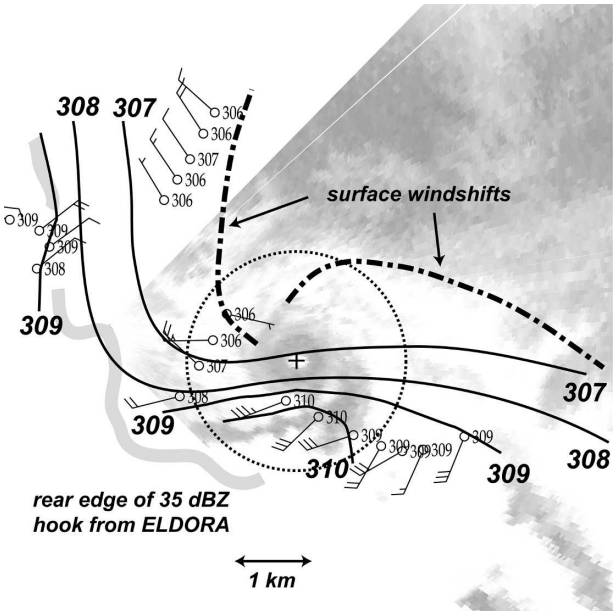

FIG. 4. Mobile mesonet and DOW radar reflectivity data near 0105:08 UTC. Mobile mesonet data ±3 min of this time (approximately 1% of the available observations in this time and space domain is shown), located by time-to-space conversion using the motion of the tornado. Symbols show wind (full barb 5 m s^{-1}; half barb 2.5 m s^{-1}) and virtual potential temperature (K). Virtual potential temperature is analyzed with solid contours. The heavy dot–dash line is a wind shift line determined from analysis of all available mobile mesonet data. Radar reflectivity in the right-hand portion of the image is from the Doppler on Wheels (DOW) mobile Doppler at 2° elevation with shading ranging from <20 dBZ (white) to ~50 dBZ (darkest gray). The rear edge of the hook was determined from objectively analyzed ELDORA data at a height of about 700 m AGL. The tornado cyclone is enclosed within the dotted circle centered on the "+" sign.

from two other sites, and comparing the dimensions of the prominent features such as funnel diameter and cloud-base height. The funnel had a northward component to its tilt, especially near the ground. The funnel width was 225 ± 15 m near the ground, increasing to 320 ± 20 m at cloud base. The reflectivity contours were located using the graphical technique described in Rasmussen et al. (2003). Note that the reflectivity void associated with the tornado center was placed to be coincident with the visible tornado axis. This was necessary because the tornado was evolving and the mobile Doppler data were obtained over a 90-s period, but the photographic image is instantaneous. This positioning technique would only introduce errors in the analysis if the reflectivity hole did not, in nature, coincide with the visible funnel. Other errors, associated with the evolution of the tornado during the volume scan period, are thought to be more significant.

Figure 3 shows that the reflectivity maximum was approximately collocated with the leading edge of the cloud-free "clear slot" about 800 m north of the tornado. The width of the clear slot increased toward the south. The $\overline{M}$ data show that at the time of the image, the maximum in low-level $\overline{M}$ was found at about 1000 m radius at 800 m AGL, expanding to about 1300 m radius near the ground. This was approximately the same radius as the typical clear slot location, suggesting an association between large angular momentum and the downdrafts associated with the clear slot.

Analysis of mobile mesonet, and mobile and airborne radar data (Fig. 4), reveals several prominent features in the vicinity of the TC. A sharp wind shift line extended westward for a short distance from near the tornado, arced northward, eastward, and then southward and southwestward away from the tornado. The position of the wind shift line was established using hundreds of mobile mesonet observations obtained continuously through the observation period, <1% of which are shown herein. The wind shift is the original rear-flank gust front, and was in nearly the same position relative to the rain curtain/spiral band as it was prior to tornado formation: about 1500 m ahead (not shown). To the rear of this northward-extending wind shift line was the stem of the hook echo, and below that was a region of very divergent surface winds. Also below this portion of the hook was a mass of somewhat cooler air. Air with larger θ_v (by ~2 K) was found to the rear of the gust front to the southeast of the tornado. In this region, near-ground reflectivities were very small

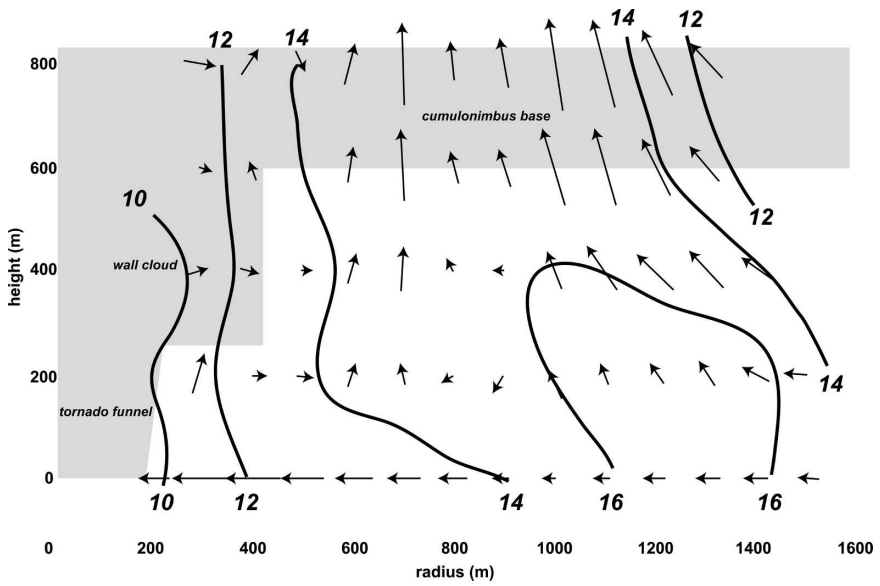

FIG. 5. Analysis of azimuthally averaged secondary flow and angular momentum from the mobile Doppler volume collected commencing 0105:12 UTC. Gray block shading denotes rough outline of azimuthally averaged cloud determined photogrammetrically (cumulonimbus base continues past 1600-m radius) and contours are $\times 10^3$ m^2 s^{-1}. The maximum vector is 8 m s^{-1}.

(often <0 dBZ), most likely associated with the presence of dry air that had descended from aloft and was relatively devoid of scatterers.

During this period of intensification of the low-level angular momentum, the secondary or meridional circulation (u, w) was dominated by inward and upward flow at most radii (Fig. 5). The exception to this was found inside 600 m radius within 400 m of the ground where the flow turned outward above an intense shallow inflow layer. A maximum in $\overline{M}$ extended from near the ground at 1400 m radius upward and inward along the sloping flow to about 800-m radius at 800-m elevation.

Certain terms of (3) can be evaluated from this analysis (Fig. 6). The terms have been grouped and evaluated as follows. The tendency of azimuthally averaged angular momentum, $\partial\overline{M}/\partial t$, shown in the top panel, was evaluated using the change in $\overline{M}$ between the 0103:32 and 0106:51 UTC volume scan analyses (centered difference in time). The mean tendency due to advection, $-\overline{u}f\overline{M}/dr - \overline{w}f\overline{M}/dz$, was evaluated as the average of this term at 0103:32, 0105:08, and 0106:51 UTC, using centered differences in space at each time. The residual, shown in the bottom panel, is the difference between the tendency and advection, and as discussed previously consists of the convergence of the eddy angular momentum flux and loss of angular momentum to the ground.

There are no data inside about 300-m radius in these analyses for two reasons. First, there is considerable uncertainty in dealiasing individual data in the strong flow near the radius of maximum winds (~150–200 m). Second, the averaging technique requires a sufficient number of samples at constant radius to decrease the uncertainty in the average to acceptable levels (as indicated by the ratio of the mean absolute error to av-

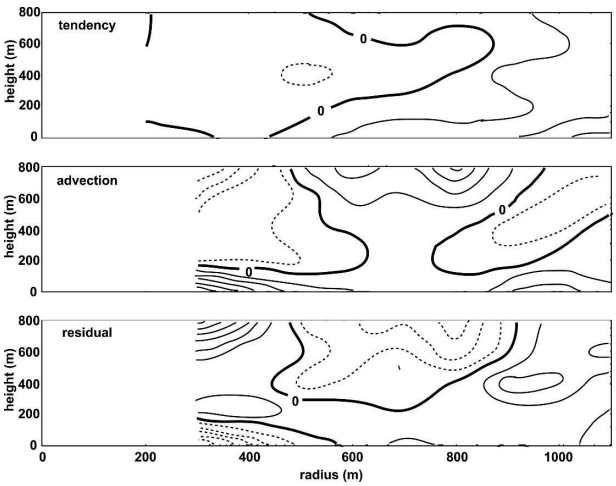

FIG. 6. Angular momentum budget (m^2 s^{-2}) during the intensifying period as described in the text: (top) the tendency term; (middle) the advection terms; (bottom) the residual. Depletion of $\overline{M}$ is indicated with broken contours; augmentation by solid contours. The contour interval is 10 m^2 s^{-2}. Gray shading denotes the approximate dimensions of the tornado and cloud features also shown in Fig. 5.

erage tangential velocity, MAE/$\bar{v} < 0.35$). Details of this inner flow are thoroughly documented in Wurman and Gill (2000).

At small radii in this period, there was very little change in $\overline{M}$ with time (Fig. 6). At $r > 400$ m, and increasing in depth with radius, the tendency was strongly positive. The small tendency at $r < 400$ m was a consequence of an interesting balance. Near the ground, where there was relatively strong inflow, advection by the mean flow was contributing strongly to increasing $\overline{M}$. However, this was almost exactly offset by terms in the residual. Being adjacent to the ground, it is likely that this negative residual owed to frictional loss of $\overline{M}$ to the ground. Just above the ground (200 m elevation and above), where the mean radial flow was outward transporting smaller $\overline{M}$ to larger radii, the residual was positive, indicating inward eddy transport of $\overline{M}$, and leading to near-steadiness in the near-tornado region. It is possible that the eddy transport was being accomplished by prominent asymmetries in the flow, such as those depicted in the analysis of mobile mesonet and reflectivity data above. At larger radii, the contribution by advection was largely positive, as can be inferred through examination of the secondary flow in Fig. 5. This is only partially offset by effects expressed in the residual, and near $r = 1000$ m, the contribution by residual effects is positive. This analysis was undertaken with the purpose if determining if the obvious, strong asymmetries seen in analyses such as Fig. 4 could be supplying angular momentum to TCs against the loss of $\overline{M}$ to the ground. Analysis of the residual terms, and the actual roles of the asymmetries in TC dynamics, must await dual-Doppler analysis at high spatial and temporal resolution from future field experiments.

During the intensifying period, above 1000 m AGL, $\overline{M}$ was nearly uniform with height inside $r = 2000$ m. This radius roughly corresponds to the region containing the clear slot. We also note that $\overline{M}$ reached its maximum values in the Electra Doppler Radar (ELDORA) data during this period. Finally, peak values of $\overline{M}$ increase with radius to 3–4 km, roughly the size of the mesocyclone.

4. Transition period: 0107–0110 UTC

The visual and reflectivity character of the tornado during the transition period, during which $\overline{M}$ peaked and began to decrease in time, is illustrated in Fig. 7. Notable in this analysis is that, at ~0108 UTC, the tornado was embedded in a more extensive region of apparent downdrafts than earlier, as evidenced by the degree of cloud erosion. About 1 km south of the tornado, low-level clouds were completely gone, and reflectivity

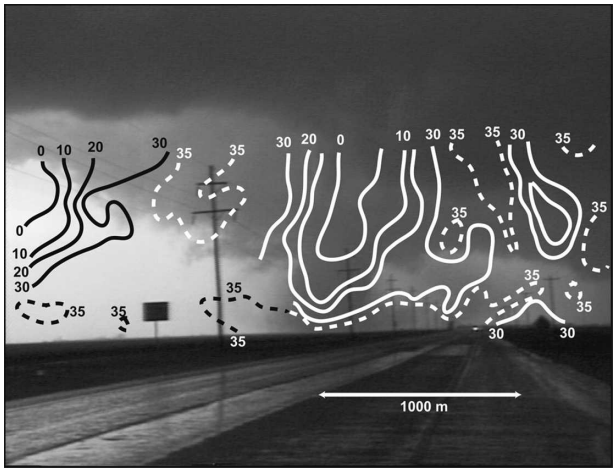

FIG. 7. As in Fig. 3, but image of the Dimmitt tornado at 0107:46 UTC digitized from Betacam video (courtesy of D. Oliver, KFDA-TV, Amarillo, TX) from east-northeast of the tornado.

in the object plane was <0 dBZ. The area filled with rain (reflectivity >30 dBZ; uncalibrated) had increased from prior times, with an extent of nearly 1 km to the south of the tornado and about 500 m to the north.

Analysis of the radar reflectivity data combined with mobile mesonet observations during this transition period reveal relatively little change from the earlier period (Fig. 8). By this time the near-tornado surface air to the southwest through north of the TC was perhaps very slightly cooler, with virtual potential temperature <306 K moving to within about 1 km of the TC. The strong temperature contrast continued to exist near the hook just south of the TC, with cooler air on the inside of the hook, and warmer and drier air in the reflectivity-sparse region just south of the hook. Very strong surface wind divergence, >0.01 s^{-1} (>10 m s^{-1} across a 1000-m wide zone in mobile mesonet data) was located directly beneath the hook to the northwest through north of the TC, and along the south edge of the hook south of the TC extending into the reflectivity-sparse area east through south of the TC (single-Doppler velocities from the mobile Doppler indicate strong divergence east of the tornado in the radar clear slot). Hence, the mobile mesonet and radar data give the impression that the tornado was nearly surrounded with low-level downdrafts, being rainy and relatively cold west through north, and dry and relatively warm south through east. There is no strong evidence of physically separate downdrafts here (i.e., rear-flank downdraft versus occlusion downdraft); the downdraft region appeared visually and in mobile mesonet data to be continuous. On the other hand, this analysis does not address forcing, which conceivably could involve distinctly different forcing mechanisms from one part of

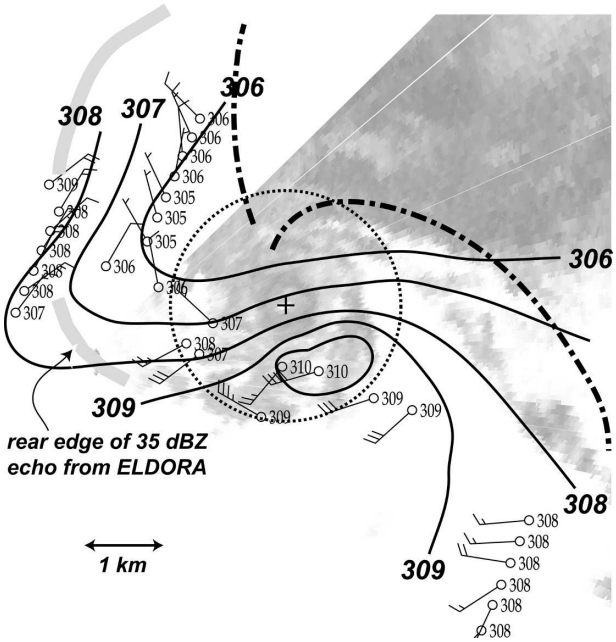

FIG. 8. As in Fig. 4, but for 0108:12 UTC.

the downdraft to another (i.e., low-level spin-induced downward-directed nonhydrostatic pressure force versus hydrometeor loading and/or evaporative cooling).

Dramatic changes occurred in the secondary circulation of the TC within a period of 2 min following the intensifying stage (Fig. 9). Although there was a remnant of azimuthally averaged updraft near $r = 800$ m, the secondary circulation was dominated by downdraft, most prominent near the tornado and beyond $r = 1000$ m. This analysis is consistent with the photographic evidence shown in Fig. 7 and the mobile mesonet observations (Fig. 8). As at earlier times, the flow turned outward above relatively intense near-ground inflow around 200 m AGL inside $r = 400$ m. The presence of downdraft outside a tornado is not necessarily detrimental to its existence from the viewpoint of angular momentum dynamics. It is possible that a downdraft could transport larger $\overline{M}$ toward the ground, and this flow could turn inward and transport $\overline{M}$ into the tornado. However, in this case, the $\overline{M}$ analysis makes it clear (especially outside $r = 1000$) that the transport due to the downdraft is bringing smaller $\overline{M}$ from aloft toward the ground. This is discussed further in section 6.

The effect of the downdraft transport can be more readily seen in Fig. 10. Except for lowest levels, the net effect of advection was to lessen $\overline{M}$ through most of the analysis domain except the lowest level. Of great interest is that the residual effects almost completely counteracted the effects of advection by the mean flow during this period, associated with near-zero tendencies everywhere between $300 < r < 1100$ m. Near the ground, as during the earlier period, the residual effects lead to lessening of $\overline{M}$, probably owing to loss to the ground through friction. However, we are unable to speculate as to what processes associated with the asymmetric parts of the flow are leading to the enhancement of $\overline{M}$ above the ground, counteracting the effects of the downdraft transport.

5. Weakening TC after 0110 UTC

During the period beginning around 0110 UTC, most photography of the Dimmitt tornado ceased. This was

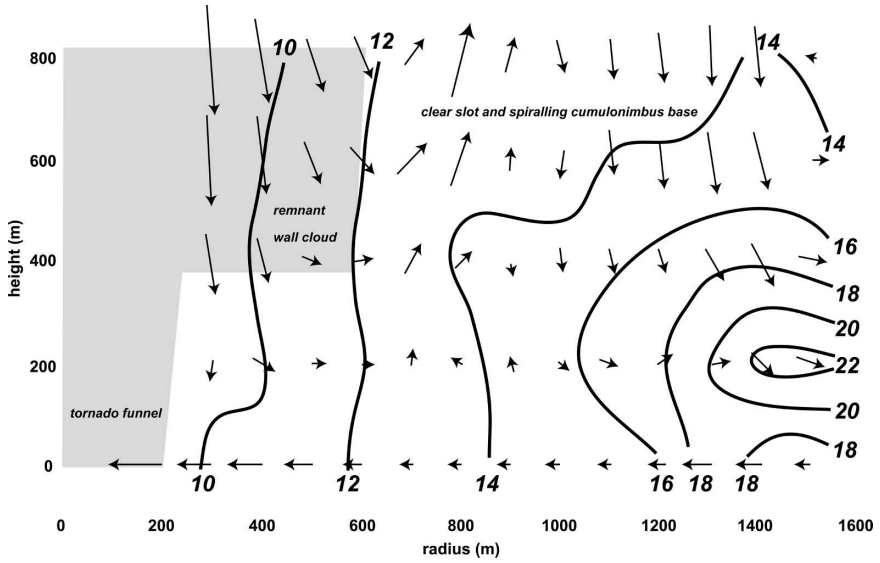

FIG. 9. As in Fig. 5, but for the transition period. See text for details.

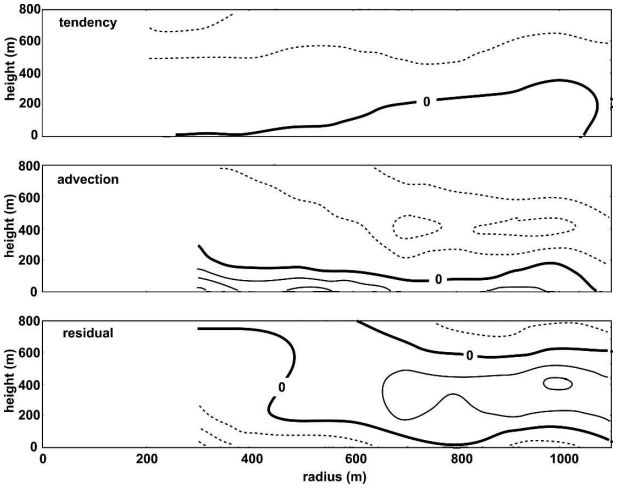

FIG. 10. As in Fig. 6, but for the transition period. Gray shading denotes the approximate dimensions of the tornado funnel and remnant wall cloud also shown in Fig. 9.

due to the motion of the tornado into the core of the storm, which made it difficult to observe from the east where most photographers were. One team of non-VORTEX chasers, Robert Prentice and Dave Gold, intercepted the tornado at a range of <1 km east of Dimmitt on Texas Highway 86. A digitized frame of their SVHS video is superimposed on a cross section of mobile Doppler reflectivity in Fig. 11. At the time the image was obtained, the near-ground reflectivity had changed somewhat from the earlier periods, with the reflectivity annulus contracting considerably in the lowest 100 m. Near the ground, relatively large reflectivity extended about 1 km south of the TC, but above the ground, reflectivity decreased sharply. This pattern could have been associated with the cessation of hydrometeor fallout.

The mobile mesonet data combined with mobile radar reflectivity indicates that near the ground the TC was embedded in a more extensive area of rain compared to previous analysis times (Fig. 12). South of the TC the observed airflow was strongly away from the tornado during this stage, consistent with the explanation that intense downdrafts had moved to a smaller radius than at earlier times. The virtual potential temperature analysis suggests that the TC is in air of about 305 K, which was only <1 K cooler than during the intensifying stage. Obviously mobile mesonet observations were not obtained very close to the tornado, so it is impossible to know the actual tornado inflow state. However, the available data do not provide much evidence that cooling of the low-level air resulted in the TC demise. The most obvious change from earlier times to the weakening stage is the apparent increase with time of downdrafts and outflow near the tornado.

This observation is further supported by the analysis of the azimuthally averaged secondary circulation (Fig. 13). The pattern of strong downward and outward flow was almost a complete reversal of the flow compared to the intensifying period. Examination of the distribution of $\overline{M}$ makes it clear that this secondary flow caused a decrease in $\overline{M}$ almost throughout the domain, as the downdrafts were transporting smaller $\overline{M}$ from aloft toward the ground. Consistent with this finding is the $\overline{M}$ tendency analysis in Fig. 14. Through most of the domain, the tendency of $\overline{M}$ had become strongly negative, and of about the same magnitude as the contribution owing to advection. As at earlier times, the residual terms contributed to decreasing $\overline{M}$ near the ground. With the near-ground air being the likely air supplying the tornado inflow, this loss of $\overline{M}$ by advection and the residual combined would almost certainly lead to the eventual demise of the tornado. In parts of the domain,

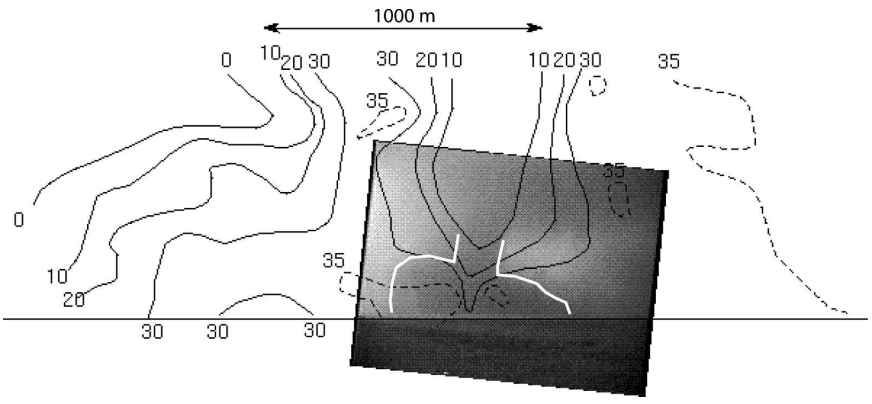

FIG. 11. As in Fig. 3, but image of the Dimmitt tornado at 0113:08 UTC digitized from S-VHS video (courtesy of R. Prentice) shot from <1 km to the southeast of the Dimmitt tornado. Bold white line is the funnel and debris cloud outline.

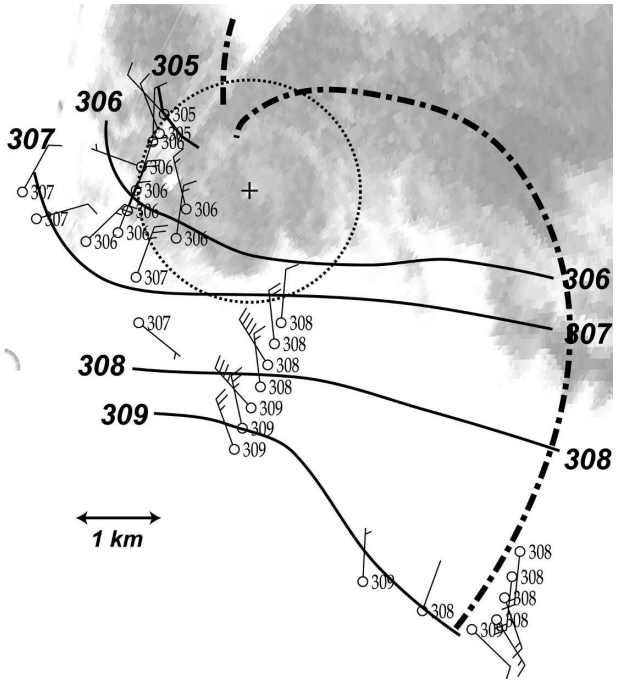

FIG. 12. As in Fig. 4, but for 0113:38 UTC. The ELDORA echo edge position is omitted because the DOW radar viewed the entire rear side of the storm. The radial bands of weaker reflectivity are due to partial beam blockage of the mobile radar.

the residual contributed to increasing $\overline{M}$, but this was insufficient to overcome the transport owing to the down-out secondary circulation.

Consideration of the raw mobile Doppler velocity data (Wurman and Gill 2000) shows that the resolvable tornado tangential velocities were roughly maintained throughout the observation period, which did not include the rope stage of the tornado. In fact, it was during the weakening period that the tornado removed all of the asphalt from Texas Highway 86 east of Dimmitt along a 40-m segment, destroyed a brick ranch home except for some of the interior hallway walls, and tossed two vehicles over 100 m.

6. Swirl as a function of height and time related to TC evolution

Changes in swirl velocity with height have been cited as being responsible for downdraft development in mesocyclones (Brandes 1984; Carbone 1983; Klemp and Rotunno 1983; Wakimoto et al. 1998). Forcing for perturbation pressure in the diagnostic pressure equation can be decomposed into parts that are a function of vorticity-squared, deformation-squared, and buoyancy. The rotational forcing acts to produce low pressure. If the largest vorticity magnitude occurs at a location above the ground, it is associated with a nonhydrostatic upward-directed pressure gradient acceleration below the vorticity maximum, and downward above. If the strongest rotation is at or near the ground, then downward-directed accelerations occur above this maximum in swirl.

The azimuthally averaged maximum resolved swirl velocity in the TC can be evaluated from raw ELDORA Doppler velocity data. To do this, the maximum inbound and outbound Doppler velocities at a radius of 800 m from the location of maximum Doppler velocity

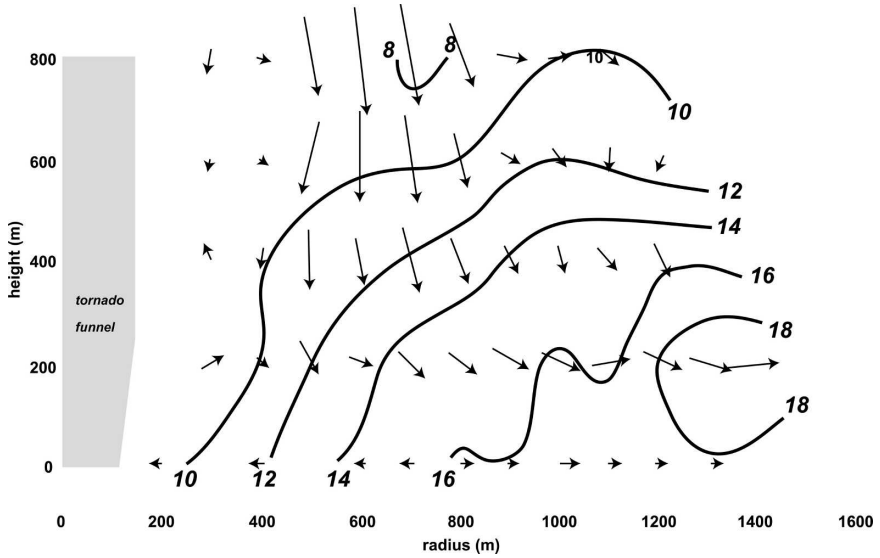

FIG. 13. As in Fig. 5, but for the weakening period. The wall cloud and cumulonimbus base were no longer apparent in or near the tornado cyclone. See text for details.

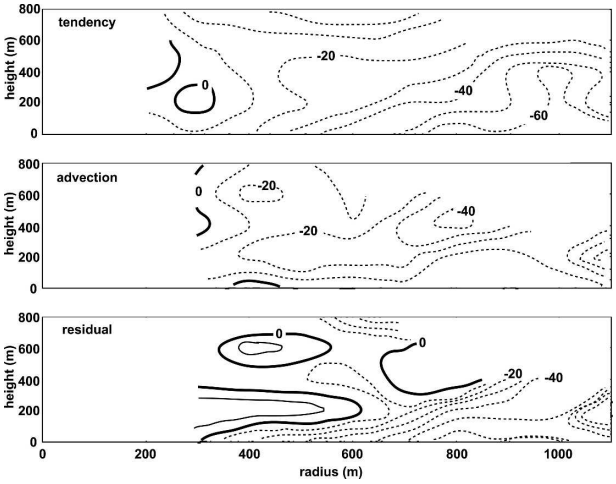

FIG. 14. As in Fig. 6, but for the weakening period. See text for details. Gray shading denotes the approximate dimensions of the tornado funnel also shown in Fig. 13.

beam-to-beam shear were subjectively interpolated for each observation time and at every 500 m in elevation commencing at 800 m AGL, the lowest well-observed level. A radius of 800 m was chosen based on the finding that downdraft formation was most pronounced at about this radius in the azimuthally averaged mobile Doppler data. Further, the radius of maximum winds changed with height and time, and was generally unresolvable in the airborne Doppler data (Brown and Wood 1997), and we seek to reduce the impact of resolution problems in this analysis.

A time–height diagram of the difference between the inbound and outbound maxima, itself a crude estimate of twice the average resolved tangential velocity and proportional to 0.5 the vertical vorticity for equivalent solid body rotation, is shown in Fig. 15. Note that the general trend of differential velocity was one of monotonic increase until about 0100 UTC, with slower monotonic weakening thereafter. Of most interest, however, is the change of differential velocity with height. During TC formation (period marked "R"), the swirl velocity was clearly largest in the lowest levels. This is somewhat misleading in that a second vortex was present aloft to the rear of the developing vortex on the gust front. However, in the near vicinity of the developing low-level vortex, the arguments above concerning the vertical pressure gradient force would imply downward accelerations. These may have been present, but likely they were far from sufficient to offset the intense upward motion that was occurring above the gust front owing to other contributions to upward accelerations. During the intensifying phase (marked "I"), it appears that the strongest swirl velocities were in general well above the ground. There is no direct evidence of wind speeds below 800 m AGL because the mobile Doppler scanning did not commence until around 0103 UTC. However, we note that during this phase the tornado was increasing in size and that when the mobile Doppler data were gathered, they showed that the angular momentum of the TC was generally increasing between 0103 and 0107 UTC. Thus, it is reasonable to surmise that the near-ground swirl was somewhat smaller than aloft, and that the vertical accelerations owing to differences in swirl with height were upward during the intensifying phase. The TC aloft reached its greatest strength at around 0100 UTC and weakened thereafter. However, mobile Doppler data indicated that a maximum in swirl velocity at 800 m radius descended from about 800 m AGL at ~0105 UTC toward the ground by 0112 UTC. Although the airborne Doppler and mobile Doppler data are not strictly comparable owing to resolution differences, at ~0103 UTC the mobile Doppler differential velocity is considerably smaller than that measured by the airborne Doppler (35–40 m s^{-1} below 800 m versus ~50 m s^{-1} at 1–2 km AGL), and by ~0110 UTC the situation is reversed with near-ground velocities considerably larger than those aloft (35–40 m s^{-1} below 400 m versus ~30 m s^{-1} above 1 km AGL). This trend suggests a reversal in the vertical nonhydrostatic pressure gradient accelerations owing to differential swirl, entirely consistent with the changes in low-level TC vertical draft structure. Therefore, the hypothesis that the formation of downdrafts in the TC was associated with differences in swirl in the vertical cannot be refuted by these data, but begs the question of what led to the changes in the vertical distribution of swirl.

7. Reflectivity in the tornado cyclone

If the buoyancy of a column of air containing a tornado cyclone were to decrease or become negative owing to hydrometeor loading and cooling from melting or evaporation, downdrafts would be expected to result. There are no means available to examine state variables related to buoyancy above the surface. Instead, the radar reflectivity is used as a proxy.

The near-ground evolution of radar reflectivity from the mobile Doppler (this is uncalibrated and may be in error by several dB) is examined in Fig. 16. The values shown are the azimuthal averages as a function of radius from the tornado center. The annulus of reflectivity >34 dBZ persisted at small radii throughout the life cycle of the TC. It increases somewhat in radius during the intensifying phase, and decreased thereafter. More relevant to TC evolution, however, is the >10 dB in-

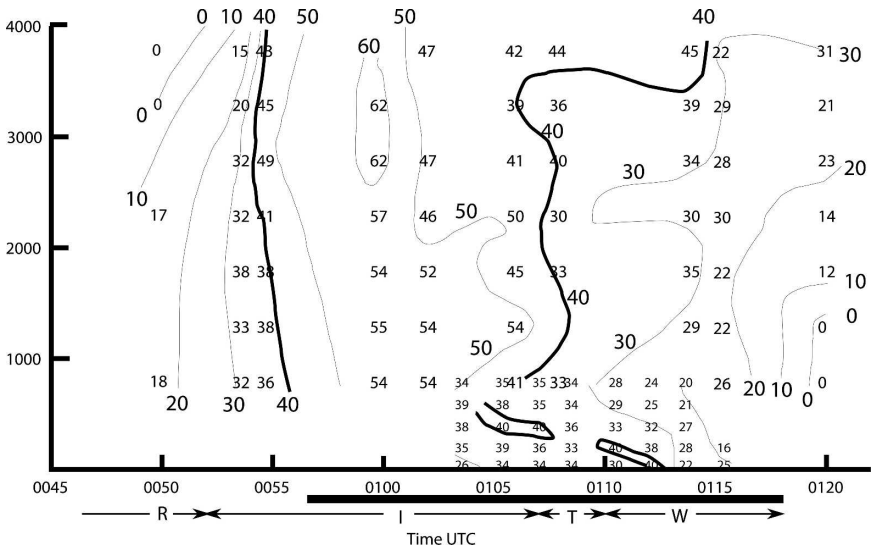

FIG. 15. Time–height diagram of tornado cyclone differential velocity (m s^{-1}) from ELDORA (above 800 m AGL). The differential was estimated at 800-m radius from the vortex center. Inset values below 1000 m AGL are the differential from the mobile Doppler at the same radius.

crease in reflectivity in the 500–1500-m radius band during the intensifying phase. Reflectivity peaked in the TC during the transition phase when downdrafts were first observed in the azimuthally averaged secondary circulation. A slow decrease in reflectivity followed during the weakening phase even though the TC was embedded in the storm core. These observations do not refute the hypothesis that water loading, and attendant decreases in buoyancy owing to evaporation and/or melting, contributed to the reversal of the TC secondary circulation.

8. Summary

This paper presents multiplatform evidence for the causes of the observed evolution of the tornado cyclone that occurred near Dimmitt, Texas, on 2 June 1995. The dynamics of the azimuthally averaged flow were examined using single Doppler data from the prototype Doppler on Wheels (DOW) mobile Doppler radar. Certain features of the evolution were clear: While azimuthally averaged angular momentum was increasing, the TC was dominated by an in-and-up secondary cir-

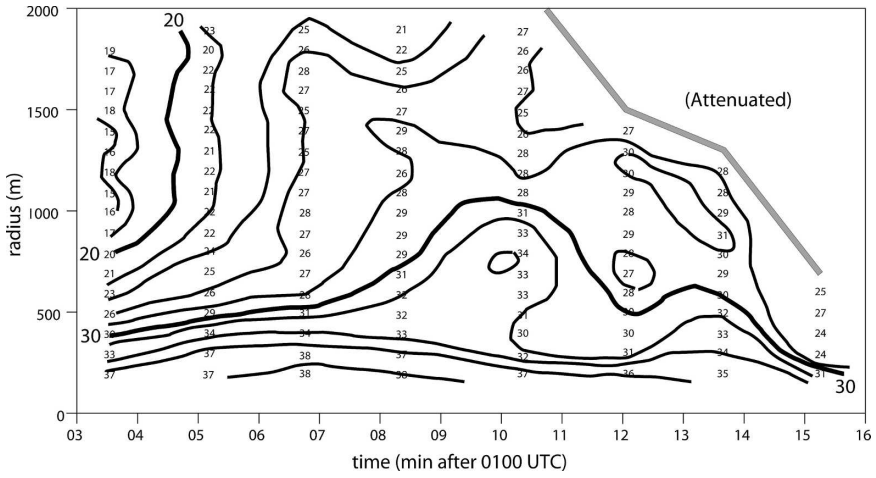

FIG. 16. Time–radius diagram of mobile Doppler azimuthally averaged reflectivity at 0° elevation angle. The contour interval is two dBZ, with 20 and 30 dBZ in heavy contours. Reflectivity factor is uncalibrated.

culation, tending to concentrate the vortex as angular momentum was quasi-conserved along streamlines. The peak intensity of the TC occurred at about the same time as the onset of downdraft just outside the tornado. With time, the secondary circulation reversed and the TC became completely dominated by a down-out configuration that transported smaller angular momentum from aloft toward the ground and outward.

In a reanalysis of the Hoecker (1961) photogrammetric study of the 1957 Dallas, Texas, tornado, Lilly (1969) found that the mean flow was contributing angular momentum near the ground and near the tornado, while removing angular momentum above the surface layer and outside the tornado. Because angular momentum was observed to increase monotonically with radius, this lead Lilly to surmise that, for the vortex to be steady, a negative viscosity effect must have been occurring in those parts of the flow in which the eddy flux was acting to increase angular momentum. Using the approach of Lilly, Rasmussen (1982) found a similar distribution and transport of angular momentum in a much more thorough photogrammetric analysis of a movie of the 28 May 1980 Lakeview, Texas, tornado. However, both studies failed to address the appropriateness of the steadiness assumption and the inability to estimate the tendency terms in the angular momentum budget. The inward eddy flux of angular momentum, because it was computed as a residual, could have been an artifact of the steadiness assumption and observational errors. In the present study, it can be seen that there are areas of inward eddy flux of angular momentum even when the tendency is accounted for. Hence, it appears that there is a negative viscosity effect occurring, and we concur with Lilly that it most likely owes to the presence of organized asymmetries such as inflow jets, the continued presence of a spiraling gust front feature, etc.

The residual terms in this budget analysis, representing the convergence of eddy angular momentum flux and loss of angular momentum to the ground, always showed the destruction of angular momentum immediately adjacent to the ground at radii generally less than 600 m, likely owing to friction. While the TC was intensifying, this destruction was offset by the transport in the average flow. Later, as downdrafts developed at ever-closer radii to the tornado axis, the azimuthally averaged flow could no longer offset the near-ground destruction. Similarly, at the levels above the ground, at early times the residual terms tended only to partially offset the base-state contributions to angular momentum. When the TC was near peak intensity and only slowly evolving, the residual terms almost exactly offset the base-state contributions, leading to a quasi-steady angular momentum distribution. But during the weakening period, the residual terms as well as the base state advection were associated with rapid weakening of the TC over most of the analysis domain.

We now summarize the hypotheses for TC evolution that we evaluated in this paper. Early in the evolution, the strongest swirl appeared to be aloft, probably in response to strong convergence and intense updrafts during the genesis stage. With time, the strongest rotation advanced toward the ground, and this was strongly associated with a reversal of the secondary circulation from in-up to down-out. It is impossible to disassociate the changes in rotation from the development of downdrafts: did the downdrafts advect the strongest rotation toward the ground to be replaced by air with less rotation aloft, or did development of stronger rotation near the ground (destruction of strong rotation aloft?) lead to downdraft development above that level? Two plausible explanations for the observed evolution can be put forth. First, it is possible that water loading in the secluded TC updraft aloft led to a reversal of the vertical flow, and the resulting advection transported smaller angular momentum downward. This represents an instability in that it would increase the downward directed vertical pressure gradient force, further enhancing the downdrafts. Second, it is possible that other forces diminished the rotation above the ground, leading to a reversal in the vertical pressure gradient force. In either case, it seems that once the strongest rotation arrived near the ground, the destruction of the TC was inevitable because the downward accelerations would eventually lead to downward advection of more weakly rotating air.

This tornado was a rather long-lived event (21 min). It seems plausible that to produce a significantly longer-lived tornado, it is probably necessary to have a continuous transport of potentially buoyant air into the TC to allow for stretching, as well as water mass removal to maintain the strongest rotation at some level above the ground. Further, if these findings are reproduced for other supercell tornadoes, it appears that TC longevity may be strongly related the initial vertical distribution of rotation and to such effects as the rate at which the TC becomes loaded with precipitation.

Acknowledgments. The VORTEX field program was supported under NSF grants and ATM 912-0009, and through the generous support of the NOAA National Severe Storms Lab and other agencies. This analysis work was supported by NSF Grants ATM 961-7318, ATM 000-3689, ATM 003-4549, and ATM-0340693. This study would have been impossible without the pioneering contributions of Dr. Joshua Wurman (Center

for Severe Weather Research) in mobile Doppler radar, and we are grateful for his ongoing efforts in tornado observations. This manuscript benefited from early reviews by Doug Lilly and Robert Davies-Jones.

REFERENCES

Bluestein, H. B., W.-C. Lee, M. Bell, C. C. Weiss, and A. L. Pazmany, 2003: Mobile Doppler radar observations of a tornado in a supercell near Bassett, Nebraska, on 5 June 1999. Part II: Tornado-vortex structure. *Mon. Wea. Rev.,* **131,** 2968–2984.

Brandes, E. A., 1984: Relationships between radar-derived thermodynamic variables and tornado genesis. *Mon. Wea. Rev.,* **112,** 1033–1052.

Brown, R. A., and V. T. Wood, 1997: Effects of radar sampling on single-Doppler velocity signatures of mesocyclones and tornadoes. *Wea. Forecasting,* **12,** 928–938.

Carbone, R. E., 1983: Severe frontal rainband. Part II: Tornado parent vortex circulation. *J. Atmos. Sci.,* **40,** 2639–2654.

Hoecker, W. H., 1961: Wind speed and airflow patterns in the Dallas tornado of April 2, 1957. *Mon. Wea. Rev.,* **88,** 167–180.

Klemp, J. B., and R. Rotunno, 1983: A study of the tornadic region within a supercell thunderstorm. *J. Atmos. Sci.,* **40,** 359–377.

Lee, W.-C., F. E. Marks, and R. E. Carbone, 1994: Velocity track display—A technique to extract real-time tropical cyclone circulations using a single airborne Doppler radar. *J. Atmos. Oceanic Technol.,* **11,** 337–356.

Lilly, D. K., 1969: Tornado dynamics. NCAR Manuscript 69-117, NCAR, 44 pp.

Markowski, P. M., 2003: Tornadogenesis resulting from the circulation transport of a downdraft: Idealized numerical simulations. *J. Atmos. Sci.,* **60,** 795–823.

——, J. M. Straka, and E. N. Rasmussen, 2002: Direct surface thermodynamic observations within the rear-flank downdrafts of nontornadic and tornadic supercells. *Mon. Wea. Rev.,* **130,** 1692–1721.

Rasmussen, E. N., 1982: The Tulia outbreak storm: Mesoscale evolution and photogrammetric analysis. Atmospheric Science Group, Texas Tech University, 180 pp.

——, J. M. Straka, R. Davies-Jones, C. A. Doswell III, F. H. Carr, M. D. Eilts, and D. R. MacGorman, 1994: Verification of the origins of rotation in tornadoes experiment: VORTEX. *Bull. Amer. Meteor. Soc.,* **75,** 995–1006.

——, R. Davies-Jones, and R. L. Holle, 2003: Terrestrial photogrammetry of weather images acquired in uncontrolled circumstances. *J. Atmos. Oceanic Technol.,* **20,** 1790–1803.

Straka, J. M., E. N. Rasmussen, and S. E. Fredrickson, 1996: A mobile mesonet for finescale meteorological observations. *J. Atmos. Oceanic Technol.,* **13,** 921–936.

Wakimoto, R. M., and B. E. Martner, 1992: Observations of a Colorado tornado. Part II: Combined photogrammetric and Doppler radar analysis. *Mon. Wea. Rev.,* **120,** 522–543.

——, C. Liu, and H. Cai, 1998: The Garden City, Kansas, storm during VORTEX 95. Part I: Overview of the storm's life cycle and mesocyclogenesis. *Mon. Wea. Rev.,* **126,** 372–392.

Wurman, J., and S. Gill, 2000: Finescale radar observations of the Dimmitt, Texas (2 June 1995), tornado. *Mon. Wea. Rev.,* **128,** 2135–2164.